Check for updates

RESEARCH ARTICLE

NANO · MICRO small
www.small-journal.com

Engineering Inorganic Perovskite Films by *X* Values of $DMAPbI_x$ toward Large Area Photovoltaic Devices by Slot-Die Coating

*Yifang Qi, Qiqi Zhang, Jeffrey Aguinaga, Chuchu Qiu, Rui Hang, Sheng He, Saroj Upreti, Antim Maurya, Nihar Pradhan, Paresh Chandra Ray, Vitor Pomin, Xiaodan Gu, Derek Patton, Tianquan Lian, and Qilin Dai**

Dimethylammonium lead iodide ($DMAPbI_x$) has the potential to address the phase stability issue of inorganic perovskite solar cells (PSCs). In this study, the crystallinity, phase structure, defect states, and crystal growth habits of $DMAPbI_x$ are controlled by adjusting the *x* value during synthesis, where N,N-dimethylacetamide (DMAC) is used as the solvent to regulate perovskite film growth. Furthermore, large-area $CsPbI_{2.85}Br_{0.15}$ perovskite films with preferred oriented growth are achieved using the optimized *x* value in $DMAPbI_x$ through the slot-die coating method. The inorganic PSCs, with a n-i-p structure and the active area of 0.04 cm^2, achieve a champion power conversion efficiency (PCE) of 19.82%, with an open-circuit voltage (V_{oc}) of 1.16 V based on perovskite films formed by slot-die coating. This work provides important insights into the $DMAPbI_x$-based method for fabricating high-quality inorganic perovskite films, and paves the way for large-area inorganic PSCs fabrication for practical applications.

1. Introduction

PSCs have attracted great attention in recent years due to low exciton binding energy, long carrier lifetime, high defect tolerance, and tunable bandgaps.[1–3] The organic–inorganic hybrid PSCs lead in terms of power conversion efficiency (PCE), and the certified efficiency of single-junction hybrid PSCs with p-i-n structure has reached 26.7%.[4] However, the poor intrinsic thermal stability of hybrid PSCs (e.g., methylammonium lead iodide, and formamidinium lead iodide) limits the industrial application, as the organic cations (FA^+ and MA^+) are volatile in perovskite films under environmental moisture, light, or heat stress.[5–8] The inorganic PSCs, with suitable bandgaps and excellent photovoltaic properties, exhibit better thermal stability than organic-inorganic hybrid PSCs.[9] Among them, $CsPbX_3$ (where X = halogen) stands out as the most promising type because Cs^+ ion is the most feasible inorganic cation to occupy ammonium sites.[8] The inorganic perovskite phases include the orthorhombic structures (γ (2H) and δ (4H)), the tetragonal structure (β (6H)) and the photovoltaically active black phase of cubic structure (α (3C)).[2,10,11] The cubic inorganic perovskite phase has a bandgap of ≈1.7 eV, which is suitable for photovoltaic device applications.[12,13] However, the effective radius of the Cs^+ ion is only 1.88 Å, resulting in a low tolerance factor of $t = 0.851$, which falls outside the range for a stable cubic perovskite structure. As a result, the cubic $CsPbI_3$ structure is unstable at room temperature.[12,14] The inorganic perovskite films could easily be converted to δ-$CsPbI_3$ with a wide bandgap of ≈2.8 eV at room temperature, leading to poor photovoltaic performance.[15,16] Therefore, it is essential to enhance the phase stability of the cubic $CsPbI_3$ perovskite film to get high efficiency and high stability of devices. $DMAPbI_x$-based perovskite precursor solution avoids undesirable phase transition of perovskite, exhibiting the significant potential to solve the stability issue of cubic $CsPbI_3$ perovskites.[17,18] Cs^+ ions are partly replaced by DMA^+ (dimethylammonium) ions to stabilize the cubic $CsPbI_3$ phase due to its effective radius of 2.72 Å.[12] Snaith et al. utilized $DMAPbI_x$ as an additive into $CsPbI_3$ perovskite precursor solution[19] to stabilize the black phase of $CsPbI_3$. Chen et al. reported inorganic $CsPbI_2Br$ PSCs with a PCE of 12.4% by $DMAPbI_x$ strategy.[18] Kanatzidis et al. incorporated $DMAPbI_x$ into inorganic $CsPbI_3$ perovskite to achieve PCE of ≈12.62%.[12] Liu group reported $CsPbI_3$ and $CsPbI_{2.8}Br_{0.2}$

Y. Qi, Q. Zhang, N. Pradhan, P. C. Ray, Q. Dai
Department of Chemistry
Physics
and Atmospheric Sciences
Jackson State University
Jackson, MS 39217, USA
E-mail: qilin.dai@jsums.edu

J. Aguinaga, S. Upreti, X. Gu, D. Patton
School of Polymer Science and Engineering
Center for Optoelectronic Materials and Devices
The University of Southern Mississippi
Hattiesburg, MS 39406, USA

C. Qiu, R. Hang, S. He, T. Lian
Department of Chemistry
Emory University
Atlanta, GA 30322, USA

A. Maurya, V. Pomin
Department of BioMolecular Sciences
University of Mississippi
University, MS 38677, USA

The ORCID identification number(s) for the author(s) of this article can be found under https://doi.org/10.1002/smll.202503825

DOI: 10.1002/smll.202503825

 © 2025 Wiley-VCH GmbH

inorganic PSCs with PCE over 20%.[20–23] Liu group also fabricated $CsPbI_{2.85}Br_{0.15}$ inorganic PSCs with $DMAPbI_x$, yielding PCE values over 21%.[24–26] Although the $DMAPbI_x$ strategy has become the most common method to improve the performance of the devices including efficiency and stability, the mechanism of $DMAPbI_x$ growth and the influence on inorganic perovskite film growth is still not clear. Most importantly, the lack of fundamental understanding of the component in terms of x values, which may optimize the perovskite component and corresponding device performance significantly, limiting the development of this method in the fabrication of inorganic PSCs.

Perovskite degradation under environmental conditions such as oxygen and moisture is associated with the nature of iodide according to ISOS protocol.[27] Oxygen-induced degradation of perovskite films is reported to reach saturation within 10 min for a 500 nm thick film.[28] Research efforts showed that the stoichiometric ratios of the final perovskite films after annealing process are different from the perovskite precursor solution.[29–31] The I to Pb ratio was reported to be 2.60-3.02:1 in 2D perovskite according to the literature.[32] Pb to I ratio was measured to be 1:1.55 for $FA_{1-x}MA_xPbI_3$ perovskite films.[33] Du et al. reported that the I to Pb ratio was less than 3 in $MAPbI_3$ perovskite films.[34] It is known that the I to Pb ratio affects the film defect states, charge transport, and energy levels of the perovskite films, which influence the corresponding PSC device performance significantly. However, the knowledge gap in understanding the relationship between the I to Pb ratios, perovskite film properties, and device performance hinders the development of film fabrication toward optimized components for high-performance devices. Moreover, the optimized ratio of I to Pb for high-quality films and high-performance devices could differ from 3:1, and the exact value remains unknown.

The efficiency record of $CsPbI_{2.85}Br_{0.15}$ inorganic PSCs was reported to be 21.08%,[24] and devices were fabricated by the spin-coating method. However, the spin-coating method is not suitable for large-area PSC fabrication, which limits its industrial applications.[35] Non-spin coating methods attracted much attention due to their significant potential in large-area PSCs for practical applications. Zhao et al. fabricated $CsPbI_2Br$ PSCs by a blade coating method, and the PCE value was 14.7% for 0.03 cm^2 active area device.[36] Vaynzof et al. reported the $CsPbI_3$ PCSs by thermal deposition, and its efficiency reached 15% for 4.5 mm^2 active area device.[37] Monroy et al. fabricated $CsPbI_3$ PSCs with an all-evaporated structure, and the PCE value of the device (0.025 cm^2) was ≈8%.[38] Qi et al. fabricated $CsPbBr_3$ inorganic PSCs via a vapor growth method, and a PCE of 10.91% was achieved for 0.09 cm^2 device.[39] Zhao et al. utilized the blade coating method to fabricate $CsPbI_3$ PSCs with an optimized PCE of 19% for an active area of 0.09 cm^2.[40] In our previous work, we fabricated $CsPbI_{2.77}Br_{0.23}$ PSCs with green solvents by slot-die coating and the PCE reached 19.05%.[41] Slot-die coating is one of the most promising methods to fabricate large-area inorganic PSCs for future industrial applications due to the low cost of manufacturing and the ability to form uniform films on rigid or flexible substrates.[35,42] In addition, slot-die coating is a pre-metered coating method, where the formation of films with predefined thickness is possible and the wastage of precursor can be minimized.[35] Therefore, the development of large-area inorganic PSCs is still very urgent for practical applications.

Herein, we control the molar ratios of PbI_2 to HI in the synthesis process of $DMAPbI_x$ using DMAC to control the defects, crystallization process, and microstructures of the $DMAPbI_x$, and to optimize the x values in $DMAPbI_x$. The inorganic perovskite films are substantially affected by the $DMAPbI_x$ synthesized with different molar ratios of PbI_2 to HI in terms of I to Pb ratios of the perovskite films, valence band maximum (VBM) positions, conduction band minimum (CBM) positions, defect states, and surface states, leading to optimized charge extraction and transport properties of devices. High efficiency of 19.82% is achieved based on our optimized perovskite films by slot-die coating method with the optimized ratio of I to Pb of 3.8:1 on the surface of the film.

2. Results and Discussions

The $DMAPbI_x$-based solution method is considered to be one of the most effective ways to avoid phase transition from perovskite to non-perovskite phase.[11,20] $DMAPbI_x$ powders are usually prepared via the chemical reaction of PbI_2, dimethylammonium (DMA^+), and HI.[12,43] The chemical reaction is shown in Equation (1).[1]

$$PbI_2 + DMA^+ + HI \rightarrow DMAPbI_X + DMAI \uparrow (g) \quad (1)$$

In this work, the x value in $DMAPbI_x$ is controlled to manipulate the growth of inorganic perovskite films via the intermediate phase/product in terms of defect states, crystallinity, and electron configuration. **Figure 1** shows the overview of this work. Three different synthetic routes to obtain $DMAPbI_x$ powders controlled by solvent and x values via the ratios of PbI_2 to HI are presented in Figure 1a left. Then $DMAPbI_x$ powders, CsI, and $PbBr_2$ were dissolved in the mixed solution of dimethylformamide (DMF) and dimethyl sulfoxide (DMSO) to form perovskite precursor solutions (Figure 1a right). Figure 1b presents a schematic of the slot-die coating of perovskite precursor solution on the top of FTO/TiO_2, followed by spiro-MeOTAD solution coated on the top of annealed perovskite films.

The molar ratio of PbI_2 to HI highly affects the synthesis phenomena, $DMAPbI_x$ component (x value), and growth of $DMAPbI_x$. **Figure 2a** shows that the $DMAPbI_x$ powders precipitate in DMAC with the molar ratios of PbI_2 to HI 1:0.5, 1:0.9, 1:1, 1:2, and 1:3, and the color of the solution changes from light-yellow to red-brown with the decrease of PbI_2 to HI ratio. The ratio of 1:0.9 is the critical ratio to obtain precipitate in the solution. A yellow transparent solution without any precipitation is formed when the molar ratio is higher than 1:0.9; for example, the solution formed at molar ratio 1:0.5 (PbI_2 to HI) in Figure 2a. $DMAPbI_x$ are obtained by filtering and washing with DE for the case of PbI_2 to HI = 1:0.5.

Figure 2b displays the X-ray diffraction (XRD) patterns of $DMAPbI_x$ powders prepared with varying ratios of PbI_2 to HI. The main peaks are observed at 11.80°, 20.45°, 26.03°, 29.97°, 31.26°, 32.32°, 41.32°, 42.07°, and 43.08°, which are consistent with previously reported literature.[12] However, new peaks at 11.16° and 17.69° are observed in XRD patterns for the molar ratio of PbI_2 to HI 1:2 and 1:3, which are attributed to the excess HI in the solution resulting in the additional phase.[44] The intensity ratio of peaks at 11.80° to 26.03° is affected by the molar ratios of

© 2025 Wiley-VCH GmbH

16136829, 2025, 33, Downloaded from https://onlinelibrary.wiley.com/doi/10.1002/smll.202503825 by University Of Pennsylvania, Wiley Online Library on [06/10/2025]. See the Terms and Conditions (https://onlinelibrary.wiley.com/terms-and-conditions) on Wiley Online Library for rules of use; OA articles are governed by the applicable Creative Commons License

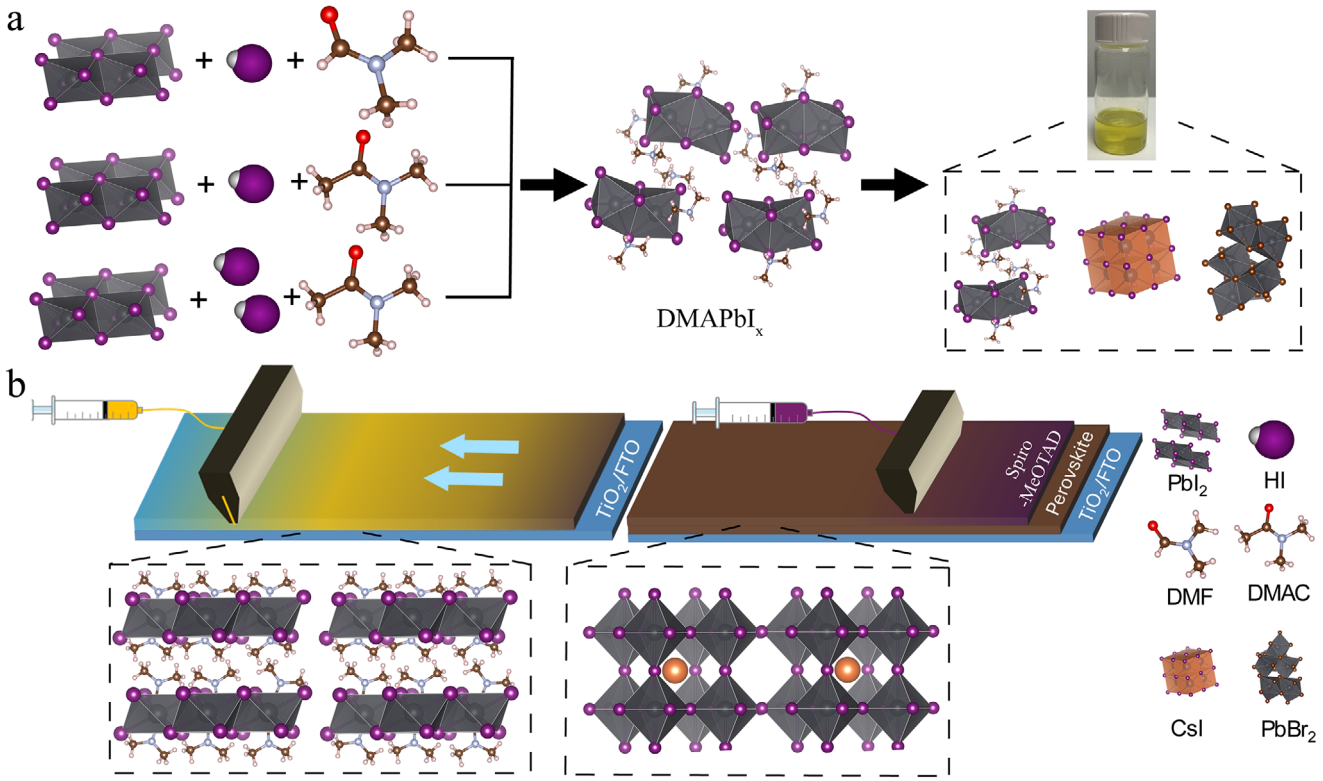

Figure 1. a) The fabrication process of perovskite precursor solution by DMAPbI$_x$ prepared with different ratios of PbI$_2$ to HI. b) Diagram of perovskite and spiro-MeOTAD layer preparation by slot-die coating.

PbI$_2$ to HI, as shown in Figure 2c. The intensity ratios of peaks at 11.80° to 26.03° increases as the ratio of PbI$_2$ to HI decreases from 1:0.5 to 1:1, then decreases as the ratios of PbI$_2$ to HI further decreases from 1:1 to 1:3, leading to the maximum peak intensity ratio value of 2.82. Therefore, the DMAPbI$_x$ crystal growth process and orientation are greatly influenced by molar ratios of PbI$_2$ to HI in the reaction.[45–47] The X-ray photoelectron spectroscopy (XPS) measurement is conducted to study the chemical states of the elements in DMAPbI$_x$ powders in Figure 2d, and also to confirm the ratios of Pb to I for the DMAPbI$_x$ powders caused by different ratios of PbI$_2$ to HI added in the DMAPbI$_x$ synthesis process. All the XPS spectra of DMAPbI$_x$ powders exhibit two peaks at 629.82 and 618.15 eV, which are attributed to I 3d$_{3/2}$ and I 3d$_{5/2}$, respectively.[48] The peaks at 142.65 eV and 137.42 eV of the XPS spectra of the DMAPbI$_x$ powders are ascribed to Pb 4f$_{5/2}$ and Pb 4f$_{7/2}$, respectively.[49]

Figure 2e shows the molar ratio of I to Pb obtained from XPS spectra of DMAPbI$_x$ powders based on different ratios of PbI$_2$ to HI. It is observed that the molar ratio of I to Pb in DMAPbI$_x$ powders increases from 1.45:1 to 3.06:1 as the ratio of PbI$_2$ to HI decreases from 1:0.5 to 1:3. The perovskite films exhibit very similar crystal structure measured by grazing incidence wide-angle X-ray scattering (GIWAXS) (Figure S1, Supporting Information), but the ratio of I to Pb in the perovskite films are different (Figure S2 and Table S1, Supporting Information), which is dictated by the components of DMAPbI$_x$ caused by the ratio of PbI$_2$ to HI. The ratio of I to Pb in our perovskite films increases from 3.5 to 5.2 as the ratio of PbI$_2$ to HI of DMAPbI$_x$ decreases from 1:0.5 to 1:3, whereas the reported ratio of I to Pb is 3.02 or less in perovskite films.[32–34] The excess HI in synthesis of DMAPbI$_x$ could have led to amorphous I-based compound on the surface of the perovskite film. And the Pb vacancy also can be occupied by I ion,[50] which might be another reason for the high ratio of I:Pb according to the literature.[32–34] The I:Br ratio of all the samples are in the range of 17.4–21.2, indicating similar bandgaps of the perovskite films with different I:Pb ratios. The ratio of PbI$_2$ to HI affects the final perovskite film composition, defect states, and microstructures, which may further influence the corresponding photovoltaic performance. We collected the XPS data based on different sputtering times to study the I to Pb ratio on different depths of the film. The optimized film with the PbI$_2$ to HI ratio of 1:1 was selected to study the I/Pb ratio across the whole film (Figure S3a,b, Supporting Information). The calculated results based on the XPS data show that the I/Pb ratio of 3.92 on the surface of the film, which is indicated by 0 nm in the figure. The I/Pb ratios are 2.99, 3.16, 3.15, and 2.95 as the sputtering depth increased to 100, 160, 220, and 300 nm, respectively. The I/Pb ratio is calculated to be 2.18 as the sputtering depth increased to 400 nm, where the Sn signal from FTO glass is observed, indicating the removal of the perovskite film by sputtering. The I/Pb ratio on the perovskite film surface is 3.92, and the I/Pb ratio inside the film is very close to the stoichiometry (3:1) of the perovskite crystal. As the sputtering process increased to 400 nm, the I/Pb ratio shows 2.18, which is consistent with the literature results.[32–34] We also sputtered the film based on the ratio of PbI$_2$ to HI = 1:0.9 (Figure S3c,d, Supporting

© 2025 Wiley-VCH GmbH

16136829, 2025, 33, Downloaded from https://onlinelibrary.wiley.com/doi/10.1002/smll.202503825 by University Of Pennsylvania, Wiley Online Library on [06/10/2025]. See the Terms and Conditions (https://onlinelibrary.wiley.com/terms-and-conditions) on Wiley Online Library for rules of use; OA articles are governed by the applicable Creative Commons License

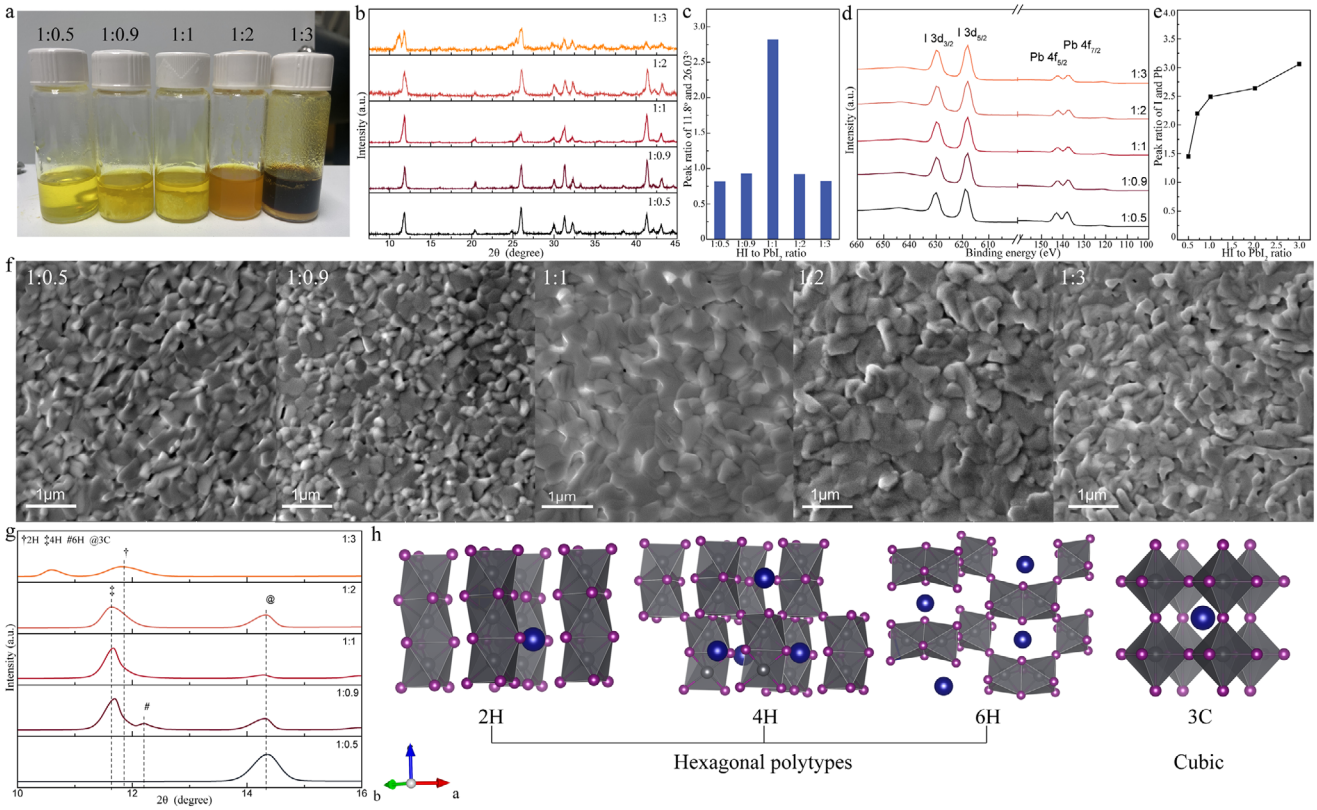

Figure 2. a) Photographs of DMAPbI$_x$ precursor solution with different molar ratios of PbI$_2$ to HI after heating 12 h (from left to right: 1:0.5, 1:0.9, 1:1, 1:2, and 1:3). b) XRD patterns of DMAPbI$_x$ powders based on different molar ratios of PbI$_2$ to HI. c) The relative intensity ratio of XRD peaks at 11.8° and 26.03° (in Figure 2b) versus the molar ratios of PbI$_2$ to HI. d) XPS scans of I 3d and Pb 4f spectral regions for perovskite films formed using different ratios of PbI$_2$ to HI. e) The molar ratio of I to Pb as determined via XPS spectra of DMAPbI$_x$ powders based on different ratios of PbI$_2$ to HI. f) SEM top-view images of perovskite films based on DMAPbI$_x$ with different molar ratios (PbI$_2$:HI). g) XRD patterns of the perovskite films showing the intermediate perovskite phases in the range of 10°–16° when films were annealed at 200 °C for 1 min only. h) Crystal structure of inorganic perovskite polytypes 2H, 4H, and 6H showing PbI$_6$ octahedra connectivity and 3C cubic perovskite structure.

Information). The I/Pb ratio of 3.85 is obtained on the surface of the film and decreased to 3.08, 3.10, 2.82, 2.46, and 1.96 as the sputtering depth increased to 110, 160, 220, 300, and 400 nm respectively. The comparison of the two samples showed that the optimized sample can maintain the stoichiometry (3:1) of perovskite crystal from 110 nm to 300 nm. However, the other sample (Figure S3c,d, Supporting Information) can only maintain the stoichiometry (3:1) of perovskite crystal from 110 to 220 nm. Usually, the stoichiometry of perovskite crystal is less than 3 according to the literature.[32–34] Our optimized sample showed more thicker layer inside the film could maintain the stoichiometry (3:1) of perovskite crystal compared to the other sample. The excess I on the surface might be associated with the surface defects. Meanwhile, the thick layer with the stoichiometry (3:1) of perovskite crystal inside the films may improve the device performance. Therefore, the films with excess I on the surface still exhibited optimized photovoltaic performance due to the thick layer of stoichiometry (3:1) of perovskite crystal inside the film. In addition, the UV–vis absorption (UV–vis) and PL spectra of perovskite films based on different DMAPbI$_x$ powders are presented in Figure S4 (Supporting Information), which show a similar peak position and further indicate the similar bandgap of perovskite films.[51] All the perovskite films exhibit identical Fourier transform infrared spectroscopy (FTIR) peak positions, indicating the same functional group vibration modes in perovskite films prepared by different DMAPbI$_x$ (Figure S5, Supporting Information). Figure 2f shows the scanning electron microscopy (SEM) images of the perovskite films based on DMAPbI$_x$ prepared with different ratio of PbI$_2$ to HI. A small number of pinholes are observed in the perovskite films with a PbI$_2$ to HI ratio of 1:0.5. Notably, the number of the pinholes decreases significantly as the ratio of PbI$_2$ to HI decreases to 1:1. The pinholes appear again in the perovskite film when the ratio of PbI$_2$ to HI increase to 1:3. The pinholes in perovskite films serve as sites for charge carrier recombination and also act as degradation centers, adversely affecting the stability and performance of the films.[52,53] Compared to the perovskite prepared by DMAPbI$_x$ based on 1:2 ratio of PbI$_2$ to HI, the perovskite film prepared with DMAPbI$_x$ based on 1:1 ratiopresent a much smoother morphology, which is beneficial to carrier charge extraction and transport in the devices.[54–56] And the photograph of inorganic perovskite films prepared by different DMAPbIx is shown in Figure S6 (Supporting Information). To understand the perovskite crystallization process affected by the ratio of PbI$_2$:HI, we prepared perovskite films based on DMAPbI$_x$ with different ratios of PbI$_2$ to HI annealed at 200 °C for a short time (1 min), which presents

© 2025 Wiley-VCH GmbH

16136829, 2025, 33, Downloaded from https://onlinelibrary.wiley.com/doi/10.1002/smll.202503825 by University Of Pennsylvania, Wiley Online Library on [06/10/2025]. See the Terms and Conditions (https://onlinelibrary.wiley.com/terms-and-conditions) on Wiley Online Library for rules of use; OA articles are governed by the applicable Creative Commons License

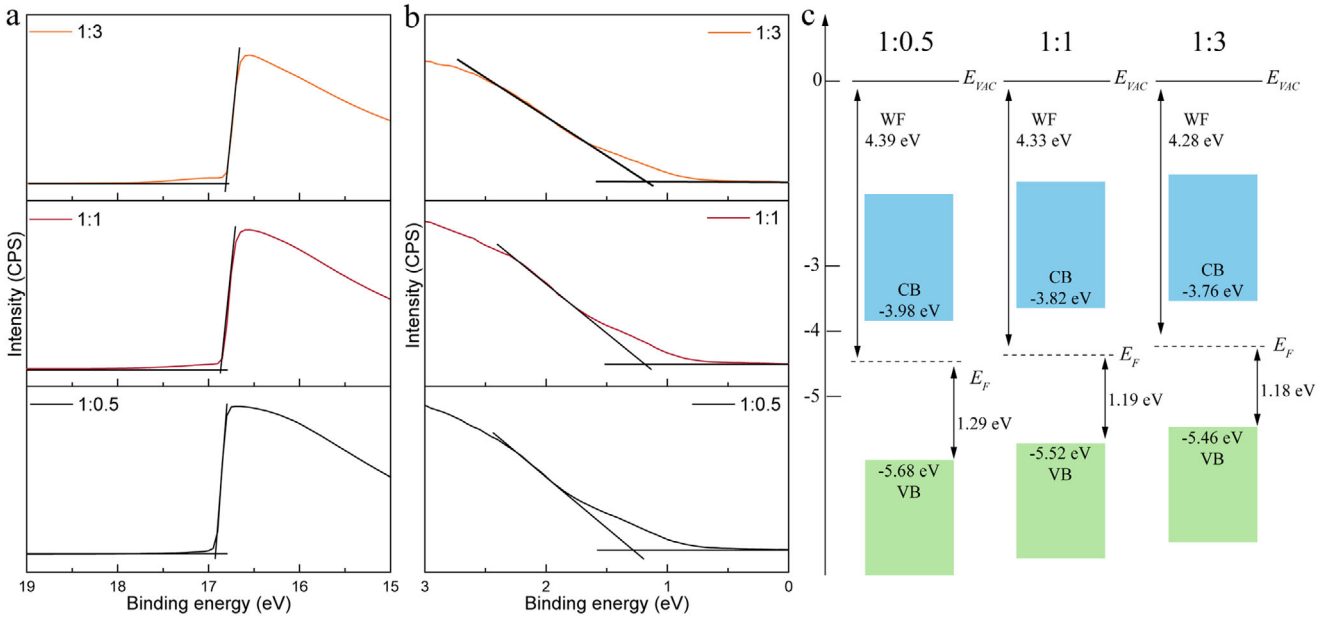

Figure 3. a,b) UPS spectra of perovskite films based on DMAPbI$_x$ with different molar ratios of PbI$_2$ to HI, and their work functions and VBMs can be derived. c) Energy level diagram of the perovskite films based on different ratios of PbI$_2$ to HI.

the conversion process to obtain the cubic (3C) perovskite crystals and allows us to study the hexagonal perovskite polytype intermediate phase during the crystallization process[57–59] (Figure 2g). The perovskite crystal structure has various polytype intermediate phases due to the stacking sequence. The yellow δ phase—also called 2H phase—is observed in the pure hexagonal closed-packed perovskite, which also has $P6_3/mmc$ space group and is composed of the face-sharing $[PbI_6]^{4+}$ octahedra separated by DMA^+ cations. 4H perovskite polytype is produced by face-sharing octahedra Pb_2X_9 (where X = halogen) and then connected to another Pb_2X_9 dimers by corner-sharing octahedra,[59] and 6H perovskite polytype exhibits a cubic phase resulting in preliminary 3D framework.[60] With increasing the molar ratio of PbI$_2$ to HI in the DMAPbI$_x$, the 2H perovskite ($2\theta \approx 11.8°$) peak disappears, while 4H($2\theta \approx 11.6°$), 6H ($2\theta \approx 12.2°$), and cubic phase ($2\theta \approx 14.2°$) peak intensities increase during the annealing process. These results suggest that perovskite crystallization sequence likely occurs from 2H, 4H, 6H and finally arrives at the 3C cubic phase as shown in Figure 2h, which is consistent with literature.[58,59] Additionally, the XRD peak appears at 10.6° may be related to the δ-phase of perovskite.[61] This result indicates it is hard to form cubic phase of perovskite when the molar ratio of PbI$_2$ to HI reaches 1:3. Therefore, the XRD patterns of the films indicates the perovskite crystallization process can be controlled by variation in the ratios of the PbI$_2$ to HI.

To further investigate the electronic structure of perovskite films based on different kinds of DMAPbI$_x$ powders, the work function (WF) and valence band minimum (VBM) were obtained by UV photoelectron spectroscopy (UPS), as shown in **Figure** 3a,b. The observed WF values are ≈16.91, 16.85, and 16.81 eV for perovskite films based on DMAPbI$_x$ with PbI$_2$ to HI ratio of 1:0.5, 1:1, and 1:3, respectively, which are determined by the secondary electron cut off.[62] In addition, the VBM positions of perovskite films based on DMAPbI$_x$ with the PbI$_2$ to HI ratio of 1:0.5, 1:1, and 1:3 are located at ≈1.18, 1.19, and 1.29 eV below the Fermi level (E_F), respectively. The energy level diagram for perovskite films based on different DMAPbI$_x$ is shown in Figure 3c. The bandgaps of perovskite films are obtained from UV–vis absorption spectra (Figure S4, Supporting Information). The VBM position shifts from −5.68 to −5.52 to −5.46 eV for the perovskite films based on DMAPbI$_x$ with PbI$_2$ to HI ratio from 1:0.5 to 1:1 and 1:3, respectively. The E_F position also shifts toward the conduction band minimum (CBM) by ≈110 meV, indicating the perovskite films based on DMAPbI$_x$ with more HI become more p-type,[63] which is beneficial for carrier charge extraction and transport to HTL.[62,64–66] Therefore, the ratio of PbI$_2$ to HI controls the electron configuration in terms of VB and CB positions of the perovskite films as well as the charge extraction and transport properties of the devices.

To investigate the influence of DMAPbI$_x$ prepared with different ratios of PbI$_2$ to HI on the PSC performance, the devices with an active area of 0.04 cm^2 were fabricated with a n-i-p stack of FTO/ TiO_2/$CsPbI_{2.85}Br_{0.15}$/spiro-MeOTAD/Au, as shown in **Figure** 4a. Figure 4b exhibits J–V curves of the champion PSCs fabricated by DMAPbI$_x$ based on various ratios of PbI$_2$ to HI, and the corresponding photovoltaic performance parameters are displayed in Table S2 (Supporting Information). The fill factor (FF) values of champion PSCs fabricated by different kinds of DMAPbI$_x$ are 1.12, 1.13, 1.16, 1.1 and 1.09 V for molar ratios of PbI$_2$ to HI 1:0.5, 1:0.9, 1:1, 1:2 and 1:3, respectively. The corresponding FF values are 76.0, 76.12, 82.4, 71.52, and 71.11%. Overall, the PCE of the devices based on different DMAPbI$_x$ powders are 16.75, 17.65, 19.82, 15.72, and 14.83%, corresponding to molar ratios of PbI$_2$ to HI 1:0.5, 1:0.9,1:1, 1:2 and 1:3 respectively. V_{oc} and FF values of the devices increase as the molar ratio of PbI$_2$ to HI decreases from 1:0.5 to 1:0.9, and these two parameters further increase and reach the optimized values as the ratio of PbI$_2$ to HI decreases to 1:1. However, the V_{oc} and FF values of

© 2025 Wiley-VCH GmbH

16136829, 2025, 33, Downloaded from https://onlinelibrary.wiley.com/doi/10.1002/smll.202503825 by University Of Pennsylvania, Wiley Online Library on [06/10/2025]. See the Terms and Conditions (https://onlinelibrary.wiley.com/terms-and-conditions) on Wiley Online Library for rules of use; OA articles are governed by the applicable Creative Commons License

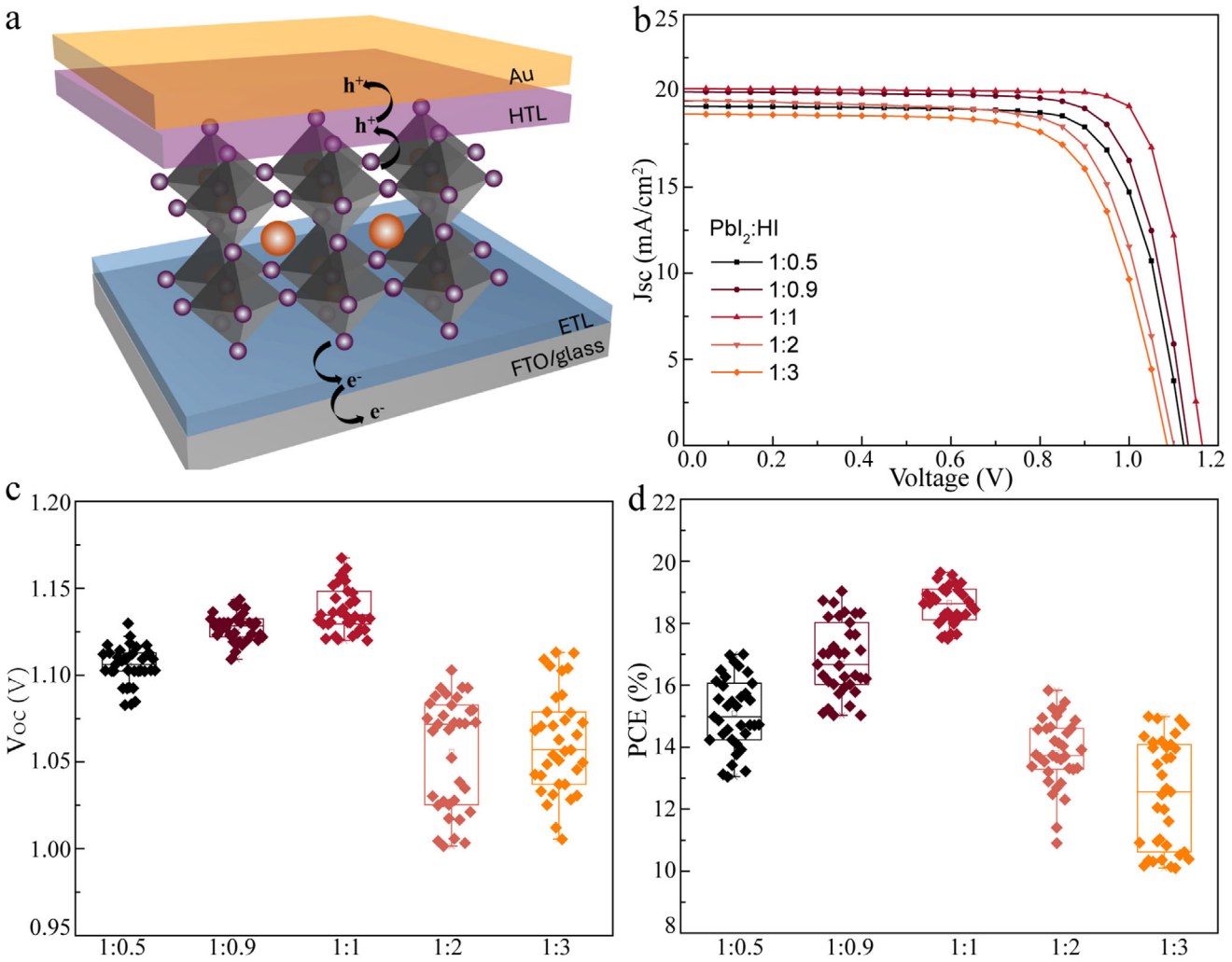

Figure 4. a) The device structure of our inorganic PSCs. b) *J–V* curves of optimized devices based on a series of $DMAPbI_x$. c,d) The reproducibility of V_{oc} and PCE of PSCs based on 35 devices prepared with the same condition for each ratio of PbI_2 to HI.

the devices decrease as the ratio of PbI_2 to HI decreases to 1:2 and 1:3. XPS results that the ratio of PbI_2 to HI affects the molar ratio of Pb to I in the final perovskite films (Figure S3 and Table S1, Supporting Information). Therefore, the performance of PSCs is significantly impacted by the amount of I in $DMAPbI_x$. The short circuit current density (J_{sc}) value of the device based on the 1:1 molar ratio of PbI_2 to HI is slightly higher than that of other devices. Therefore, the molar ratio of 1:1 for PbI_2 to HI in $DMAPbI_x$ yields the optimized performance of PSCs.

The reproducibilities of device V_{oc} and PCE performance are exhibited in Figure 4c,d. Statistical V_{oc} and PCE distributions of 35 devices are prepared with different $DMAPbI_x$ powders (controlled by the ratios of PbI_2 to HI). The average PCE value of the devices enhances from 15 to 18.5% as the ratio decreases from 1:0.5 to 1:1, and then decreases to 14% and 13% corresponding to 1:2 and 1:3, respectively, which is mainly attributed to the change of V_{oc} affected by the ratio of PbI_2 to HI. The average V_{oc} value of devices increases from 1.10 to 1.13 V when the ratio of PbI_2 to HI decreases from 1:0.5 to 1.1. Then, the average V_{oc} drops to 1.07 V and 1.05 V for the ratio 1:2 and 1:3, respectively. In addition, the small deviation for the performance of PSCs based on the molar ratio of PbI_2 to HI 1:1 indicates high reproducibility of the devices. All the results demonstrate the PSCs based on $DMAPbI_x$ synthesized by the molar ratio of PbI_2 to HI 1:1 exhibit optimized device performance compared to the devices based on other molar ratios. The optimized performance of the devices based on the molar ratio of PbI_2 to HI = 1:1 is attributed to the optimal perovskite films such as low defects density, optimized energy levels and improved charge extraction from perovskite layers possibly caused by the crystal structure, crystallinity, components of $DMAPbI_x$ in the synthesis process due to the critical ratio PbI_2 to HI.

The defects at the perovskite surface and grain boundaries influence the carrier charge transport and recombination properties dramatically. Density functional theory (DFT) calculations were carried out to further study the trap densities in the perovskite films based on different kinds of $DMAPbI_x$. The projected density of states (PDOS) is calculated by DFT level with exchange-correlation energy approximated by Perdew–Burke–Ernzerh generalized gradient approximation (PBE-GGA) simulations on

© 2025 Wiley-VCH GmbH

16136829, 2025, 33, Downloaded from https://onlinelibrary.wiley.com/doi/10.1002/smll.202503825 by University Of Pennsylvania, Wiley Online Library on [06/10/2025]. See the Terms and Conditions (https://onlinelibrary.wiley.com/terms-and-conditions) on Wiley Online Library for rules of use; OA articles are governed by the applicable Creative Commons License

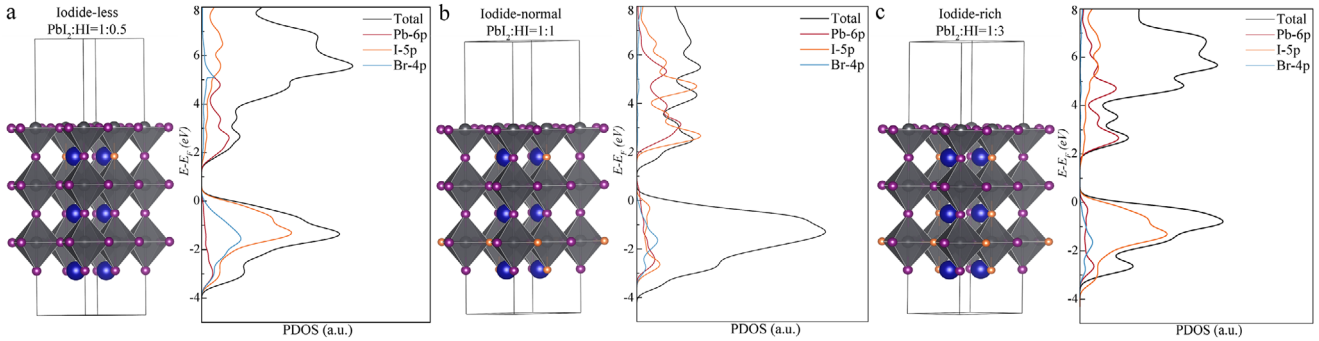

Figure 5. a–c) DFT calculation of the trap states for perovskite with a) I-less, b) I-normal, and c) I-rich, optimized crystal structures (left panel) with contributions from Br (orange), I (purple), and Pb (dark blue) and PDOS (right panel).

a 2×2×2 perovskite slab on the exposed (100) surface.[67] The CBM is dominated by the 6p orbitals of Pb element, and the VBM is chiefly contributed by the 5p orbitals of I elements (**Figure 5a**). The density of states (DOS) for perovskite films is close to the VBM due to the origin of the same iodine 5p orbitals.[68] The total DOS of I-poor and I-rich are higher than the I-normal perovskite films, as shown in Figure S7 (Supporting Information). High defect densities would induce uncoordinated Pb defects which may result in nonradiative recombination and poor device performance.[69] Additionally, PDOS spectra of the I-rich, I-less, and I-normal perovskite films (100) surface are separated into different components, as shown in Figure 5a–c. The calculated I-5p defect density states are much lower than other elements for I-less and I-rich in perovskite (100) surfaces. However, the contribution of the I and Br defect states to the calculated total DOS of the I-normal perovskite film are similar to each other (Figure 5b). Overall, both I-rich and I-less in the perovskite films may result in high defect densities, leading to charge recombination at the traps.

Traditionally, DMF reacted with HI and PbI_2 to obtain $DMAPbI_x$ powders, which was reported by literature.[70] We used DMAC to replace DMF to prepare $DMAPbI_x$ powders in this work. We controlled the ratio of HI and PbI_2 to control the $DMAPbI_x$ powder synthesis, and we did not change the DMAC amount in the $DMAPbI_x$ powder synthesis. Two kinds of $DMAPbI_x$ powders were obtained by DMF and DMAC separately. Then two kinds of $DMAPbI_x$ powders were used to fabricate perovskite films and devices. We compared the $DMAPbI_x$ powders, films, and devices obtained by the two methods (our DMAC method and traditional DMF method), and the results and the corresponding discussion are shown in Figures S8–S21 (Supporting Information). The results show the efficiency and stability of devices prepared with DMAC-$DMAPbI_x$ are better than the devices prepared with DMF-$DMAPbI_x$. A champion PCE of 19.82%, with a V_{oc} of 1.16 V was obtained by the DMAC method (Figure S13, Supporting Information). Therefore, $DMAPbI_x$ synthesized by DMAC exhibits a promising way to fabricate the inorganic perovskite solar cells.

3. Conclusions

In summary, we controlled the growth and crystal phase of $DMAPbI_x$ by different coordination solvents (DMAC and DMF) with PbI_2 to achieve the self-precipitation $DMAPbI_x$. In addition, the growth and the intermediate phase of inorganic perovskite films were further studied by $DMAPbI_x$ prepared with DMF and DMAC, affecting nucleation rates and preferred orientation growth. Introducing DMAC-prepared $DMAPbI_x$ crystals into the perovskite precursor solutions stabilized the cubic phase of inorganic perovskite, which was then prepared by slot-die coating under ambient conditions. The I to Pb ratio of the perovskite films were significantly affected by the x values in $DMAPbI_x$. Furthermore, the inorganic PSCs based on the ratio of I:Pb = 3.8 presents the champion efficiency of 19.82% and V_{oc} of 1.16 V. The stability of the PSCs based on DMAC-$DMAPbI_x$ exhibited over 80% of initial PCE after 1000 h under 15%–20% RH and temperature of 30 °C (ISOS-D-1). The DMAC-$DMAPbI_x$ device also could maintain ≈50% of the beginning PCE under the temperature of 85 °C and 20% RH (ISOS-D-2). Therefore, this work offers a comprehensive study of $DMAPbI_x$ and its effect on the growth and crystallization processes of inorganic perovskite, providing a promising approach to achieve high efficiency and stability in inorganic PSCs.

4. Experimental Section

Materials: Dimethylformamide (DMF) anhydrous, 99.8%, dimethyl sulfoxide (DMSO) anhydrous, 99.8%, spiro-MeOTAD (99%), hydriodic acid (57 wt% in H_2O, 99.95%), 4-tert-butylpyridine (4-tBP, 98%), diethyl ether (DE, 99.0%, with BHT as inhibitor), and chlorobenzene (CB), anhydrous 99.8% were purchased from Sigma-Aldrich. Lead iodide (PbI_2, 98.5%), cesium iodide (CsI, 99%), lead bromide ($PbBr_2$, 99%), lithium bis (trifluoromethanesulfonyl) imide (Li-TFSI) and dimethylacetamide (DMAC, 99%) were purchased from TCI America. Titanium (IV) chloride ($TiCl_4$), 99.0% was purchased from Fisher Scientific Chemicals. Patterned fluorine-doped tin oxide (FTO) glass substrates (≈15 Ω per sq) were obtained from Advanced Election Technology Co., Ltd.

Synthesis of $DMAPbI_x$ powders: $DMAPbI_x$ powders were prepared by two methods based on two solvents DMF and DMAC in this work. In the DMAC-based method, $DMAPbI_x$ solution was prepared by addition of PbI_2 and hydroiodic acid (with different molar ratios of 1:0.5, 1:0.9, 1:1, 1:2, and 1:3) into DMAC with stirring for 1 h. In the DMF-based method, $DMAPbI_x$ solution was prepared by addition of PbI_2 and hydroiodic acid with a molar ratio of 1:1 into DMF with stirring for 1 h. Then the solutions were kept in an oil bath at 120 °C (10 h) for DMAC or 100 °C (2 h) for DMF and the solution color changed to light yellow. For the DMAC method, $DMAPbI_x$ needle-like powders appeared as the solution temperature decreased, while there is no $DMAPbI_x$ precipitant in the DMF method.

© 2025 Wiley-VCH GmbH

16136829, 2025, 33, Downloaded from https://onlinelibrary.wiley.com/doi/10.1002/smll.202503825 by University Of Pennsylvania, Wiley Online Library on [06/10/2025]. See the Terms and Conditions (https://onlinelibrary.wiley.com/terms-and-conditions) on Wiley Online Library for rules of use; OA articles are governed by the applicable Creative Commons License

Finally, the powders were washed with DE until the supernatant turned colorless. The $DMAPbI_x$ powders were obtained after drying in the vacuum oven at 60 °C overnight.

Device Fabrication: 10 cm × 10 cm FTO substrates were cleaned by ultrasonic bath for 15 min using a detergent solution, acetone, deionized water, and isopropanol. The electron transport layer TiO_2 was prepared by the chemical bath deposition method.[71] 60.4 mL $TiCl_4$ was slowly dropped into 300 mL ice water and then the FTO substrates were immersed into the $TiCl_4$ solution at 70 °C. After 40 min, the FTO substrates were washed with deionized water and ethanol to remove the excess physisorbed TiO_2 nanoparticles. Then the FTO substrates were annealed at 200 °C for 30 min. The perovskite precursor solution was prepared by adding CsI, $PbBr_2$, and synthesized $DMAPbI_x$ powders (with molar ratio of 1: 0.15: 2.85) to 1 mL solution of DMF: DMSO (9:1 v/v), then the prepared solutions were stirred for 4 h for dissolution. Any undissolved material in the precursor solutions was removed by a 0.45 µm filter. The perovskite films were fabricated by slot-die coater (MSK-AFA-PD100, Kejing Star Technology Company) in the air glove box with the relative humidity of 20–25% and temperature of ≈25 °C, which are important factors to device efficiency. The film coating speed, coating gap, bed temperature, and precursor solution flow rate were 5 mm s^{-1}, 120 µm, 40 °C, and 3 mm s^{-1}, respectively. The wet films were annealed at 210 °C for 5 min to obtain perovskite films. After that, the spiro-OMeTAD layer was slot-die coated on the surface of perovskite films (coating speed 5 mm s^{-1}, coating gap 80 µm, solution flow rate 3 mm s^{-1}). The spiro-OMeTAD solution was prepared with 90 mg spiro-OMeTAD in 1 mL in CB with 36 µL 4tBP and 22 µL Li-TFSI solution (520 mg mL^{-1} in ACN). The slot-die coating area is 10 cm × 10 cm which has been cut for small area single device. Finally, the gold electrode layer with a thickness of 80 nm was deposited on the surface of the spiro-OMeTAD layer, and device fabrication was finished via thermal evaporation under a high vacuum of 1×10^{-4} Pa. The video in the supporting inforamtion shows the slot-die process.

Characterization: Experimental parameters for scanning electron microscopy (SEM), atomic force microscopy (AFM), UV–vis absorption spectra (UV–vis), current density–voltage (*J–V*) curve, light stability, time-resolved photoluminescence (TRPL), photoluminescence (PL), external quantum efficiency (EQE), electrochemical impedance spectroscopy (EIS), X-ray diffraction (XRD) patterns, Fourier transform infrared spectroscopy (FTIR), the grazing-incidence wide-angle X-ray scattering (GIWAXS), X-ray photoelectron spectroscopy (XPS), ultraviolet photoelectron spectroscopy (UPS) are the same as described in the previous report.[49,72,73] Femtosecond transient absorption (TA) measurements were based on a regenerative amplified Ti:Sapphire femtosecond laser system to generate the 800 nm fundamental pulse (Astrella, Coherent, 800 nm, 1 kHz, 35 fs pulse duration, and 5.1 mJ per pulse), which was split by a 90:10 beam splitter. For the 10% fundamental pulse, half of it was attenuated by a neutral-density filter and focused onto a constantly translating CaF_2 crystal to generate a white light probe pulse from 400 to 800 nm. For the 90% of the fundamental beam, half of it was used to pump a visible optical parameter amplifier (OPA, Light Conversion LLC) to generate the pump pulse at 400 nm by second harmonic generation in a type I BBO crystal. The pump pulse was chopped at 500 Hz to achieve pump-on and pump-off contrast. The power of pump pulse was controlled by a series of neutral-density filters. The delay time between pump and probe pulses was achieved by delaying the pump pulse with a delay stage. The probe and reference beams were collected by fibers and guided into grating and CMOS detector (Ultrafast System, Helios). Data collection was completed in the Helios software. NMR data were processed and analyzed by using MestReNova 14.1.0 and TopSpin 3.6.4. software (Bruker). In the sample preparation and measurement, about 30 mg of DMF-$DMAPbI_x$ and DMAC-$DMAPbI_x$ were dissolved in 550 µL of DMSO-d6 and transferred to 5 mm NMR tubes. ^1H and ^{13}C NMR experiments were performed at 25 °C on 600 MHz Bruker Avance III HD using a 5 mm BBFO RT probe equipped with Z gradient. ^1H NMR spectra were recorded using the following settings: relaxation delay of 1.0 s, acquisition time of 2.7 s, spectral width of 20.0 ppm, and 128 scans. ^{13}C spectra of related compounds were acquired using the following parameters: relaxation delay of 3.0 s, FID data points 65536 and 1024 scans.

Density functional theory (DFT) calculations were carried out carried on CP2K software to further study the trap densities in the perovskite films based on different kinds of $DMAPbI_x$. The projected density of states (PDOS) is calculated by DFT level with exchange-correlation energy approximated by Perdew–Burke–Ernzerh generalized gradient approximation (PBE-GGA) simulations on a 2×2×2 perovskite slab on the exposed (100) surface.

Supporting Information

Supporting Information is available from the Wiley Online Library or from the author.

Acknowledgements

This work was supported by National Science Foundation (DMR-2242467). The ultrafast spectroscopy measurement was supported by National Science Foundation (OIA-2326788). Q.Z. is supported by NSF-PREM grant (NSF-PREM-2423854). The steady-state PL and TRPL was supported by National Science Foundation (Award# 1900047). S.U. and X.G. thank NSF grant OIA-1757220 for providing financial support for 2D GIWAXS measurements. T.L. acknowledges support from the National Science Foundation (CHE-2305112). Y.Q. is partially supported by Princeton Alliance for Collaborative Research and Innovation.

Conflict of Interest

The authors declare no conflict of interest.

Data Availability Statement

The data that support the findings of this study are available from the corresponding author upon reasonable request.

Keywords

$DMAPbI_x$, inorganic perovskite solar cells, N,N-dimethylacetamide, slot die coating

Received: March 25, 2025
Revised: June 6, 2025
Published online: June 20, 2025

[1] H. Bian, H. Wang, Z. Li, F. Zhou, Y. Xu, H. Zhang, Q. Wang, L. Ding, S. (F.) Liu, Z. Jin, *Adv. Sci.* **2020**, *7*, 1902868.
[2] L. Duan, H. Zhang, M. Liu, M. Grätzel, J. Luo, *ACS Energy Lett.* **2022**, *7*, 2911.
[3] S. S. Mali, J. V. Patil, J.-Y. Shao, Y.-W. Zhong, S. R. Rondiya, N. Y. Dzade, C. K. Hong, *Nat. Energy* **2023**, *8*, 989.
[4] "NREL," https://www.nrel.gov/pv/cell-efficiency.html, (accessed: October 2025).
[5] K. Liu, S. Rafique, S. F. Musolino, Z. Cai, F. Liu, X. Li, Y. Yuan, Q. Bao, Y. Yang, J. Chu, X. Peng, C. Nie, W. Yuan, S. Zhang, J. Wang, Y. Pan, H. Zhang, X. Cai, Z. Shi, C. Li, H. Wang, L. Deng, T. Hu, Y. Wang, Y. Wang, S. Chen, L. Shi, P. Ayala, J. E. Wulff, A. Yu, et al., *Joule* **2023**, *7*, 1033.
[6] H. Zhang, L. Pfeifer, S. M. Zakeeruddin, J. Chu, M. Grätzel, *Nat. Rev. Chem.* **2023**, *7*, 632.

 © 2025 Wiley-VCH GmbH

16136829, 2025, 33, Downloaded from https://onlinelibrary.wiley.com/doi/10.1002/smll.202503825 by University Of Pennsylvania, Wiley Online Library on [06/10/2025]. See the Terms and Conditions (https://onlinelibrary.wiley.com/terms-and-conditions) on Wiley Online Library for rules of use; OA articles are governed by the applicable Creative Commons License

[7] H. Liu, T. Liu, X. Wang, G. Hu, B. Zheng, X. Yu, Y. Wang, D. Yang, *Adv. Energy Mater.* **2024**, *14*, 2401809.
[8] J.-K. Sun, S. Huang, X.-Z. Liu, Q. Xu, Q.-H. Zhang, W.-J. Jiang, D.-J. Xue, J.-C. Xu, J.-Y. Ma, J. Ding, Q.-Q. Ge, L. Gu, X.-H. Fang, H.-Z. Zhong, J.-S. Hu, L.-J. Wan, *J. Am. Chem. Soc.* **2018**, *140*, 11705.
[9] R. He, S. Ren, C. Chen, Z. Yi, Y. Luo, H. Lai, W. Wang, G. Zeng, X. Hao, Y. Wang, J. Zhang, C. Wang, L. Wu, F. Fu, D. Zhao, *Energy Environ. Sci.* **2021**, *14*, 5723.
[10] W. Chen, X. Li, Y. Li, Y. Li, *Energy Environ. Sci.* **2020**, *13*, 1971.
[11] W. Xiang, S. (F.) Liu, W. Tress, *Angew. Chem.* **2021**, *133*, 26644.
[12] W. Ke, I. Spanopoulos, C. C. Stoumpos, M. G. Kanatzidis, *Nat. Commun.* **2018**, *9*, 4785.
[13] A. Marronnier, G. Roma, S. Boyer-Richard, L. Pedesseau, J.-M. Jancu, Y. Bonnassieux, C. Katan, C. C. Stoumpos, M. G. Kanatzidis, J. Even, *ACS Nano* **2018**, *12*, 3477.
[14] D. B. Straus, S. Guo, A. M. M. Abeykoon, R. J. Cava, *Adv. Mater.* **2020**, *32*, 2001069.
[15] M. B. Faheem, B. Khan, C. Feng, M. U. Farooq, F. Raziq, Y. Xiao, Y. Li, *ACS Energy Lett.* **2019**, *5*, 290.
[16] E. M. Sanehira, A. R. Marshall, J. A. Christians, S. P. Harvey, P. N. Ciesielski, L. M. Wheeler, P. Schulz, L. Y. Lin, M. C. Beard, J. M. Luther, *Sci. Adv.* **2017**, *3*, eaao4204.
[17] T. Zhang, M. I. Dar, G. Li, F. Xu, N. Guo, M. Grätzel, Y. Zhao, *Sci. Adv.* **2017**, *3*, 1700841.
[18] Y. Jiang, J. Yuan, Y. Ni, J. Yang, Y. Wang, T. Jiu, M. Yuan, J. Chen, *Joule* **2018**, *2*, 1356.
[19] G. E. Eperon, G. M. Paternò, R. J. Sutton, A. Zampetti, A. A. Haghighirad, F. Cacialli, H. J. Snaith, *J. Mater. Chem. A* **2015**, *3*, 19688.
[20] T. Xu, W. Xiang, J. Yang, D. J. Kubicki, W. Tress, T. Chen, Z. Fang, Y. Liu, S. Liu, *Adv. Mater.* **2023**, *35*, 2303346.
[21] J. Wang, Y. Che, Y. Duan, Z. Liu, S. Yang, D. Xu, Z. Fang, X. Lei, Y. Li, S. (F.) Liu, *Adv. Mater.* **2023**, *35*, 2210223.
[22] J. Zhang, B. Che, W. Zhao, Y. Fang, R. Han, Y. Yang, J. Liu, T. Yang, T. Chen, N. Yuan, J. Ding, S. (F.) Liu, *Adv. Mater.* **2022**, *34*, 2202735.
[23] Y. Che, Z. Liu, Y. Duan, J. Wang, S. Yang, D. Xu, W. Xiang, T. Wang, N. Yuan, J. Ding, S. (F.) Liu, *Angew. Chem., Int. Ed.* **2022**, *61*, 202205012.
[24] Y. Liu, T. Xu, Z. Xu, H. Zhang, T. Yang, Z. Wang, W. Xiang, S. Liu, *Adv. Mater.* **2023**, *36*, 2306982.
[25] Y. Liu, W. Xiang, T. Xu, H. Zhang, H. Xu, Y. Zhang, W. Qi, L. Liu, T. Yang, Z. Wang, S. Liu, *Small* **2023**, *19*, 2304190.
[26] H. Zhang, W. Xiang, X. Zuo, X. Gu, S. Zhang, Y. Du, Z. Wang, Y. Liu, H. Wu, P. Wang, Q. Cui, H. Su, Q. Tian, S. (F.) Liu, *Angew. Chem.* **2022**, *135*, e202216634.
[27] H. Yang, X. Li, X. Guo, C. Lu, H. Yuan, A. Liu, W. Zhang, J. Fang, *ACS Energy Lett.* **2023**, *8*, 3793.
[28] N. Aristidou, C. Eames, I. Sanchez-Molina, X. Bu, J. Kosco, M. S. Islam, S. A. Haque, *Nat. Commun.* **2017**, *8*, 15218.
[29] N. Li, Y. Luo, Z. Chen, X. Niu, X. Zhang, J. Lu, R. Kumar, J. Jiang, H. Liu, X. Guo, B. Lai, G. Brocks, Q. Chen, S. Tao, D. P. Fenning, H. Zhou, *Joule* **2020**, *4*, 1743.
[30] J.-P. Correa-Baena, Y. Luo, T. M. Brenner, J. Snaider, S. Sun, X. Li, M. A. Jensen, N. T. P. Hartono, L. Nienhaus, S. Wieghold, J. R. Poindexter, S. Wang, Y. S. Meng, T. Wang, B. Lai, M. V. Holt, Z. Cai, M. G. Bawendi, L. Huang, T. Buonassisi, D. P. Fenning, *Science* **2019**, *363*, 627.
[31] Y. Chen, Q. Meng, Y. Xiao, X. Zhang, J. Sun, C. B. Han, H. Gao, Y. Zhang, Y. Lu, H. Yan, *ACS Appl. Mater. Interfaces* **2019**, *11*, 44101.
[32] Y. Li, E. L. Lim, Y. Zhang, T. Kong, X. Liu, J. Song, H. Xie, D. Bi, *ACS Appl. Energy Mater.* **2022**, *5*, 15233.
[33] Q. Jiang, Y. Zhao, X. Zhang, X. Yang, Y. Chen, Z. Chu, Q. Ye, X. Li, Z. Yin, J. You, *Nat. Photonics* **2019**, *13*, 460.
[34] T. Du, S. R. Ratnasingham, F. U. Kosasih, T. J. Macdonald, L. Mohan, A. Augurio, H. Ahli, C. Lin, S. Xu, W. Xu, R. Binions, C. Ducati, J. R. Durrant, J. Briscoe, M. A. McLachlan, *Adv. Energy Mater.* **2021**, *11*, 2101420.
[35] J. T. Matondo, H. Hu, Y. Ding, M. Mateen, G. Cheng, J. Ding, *Adv. Mater. Technol.* **2024**, *9*, 2302082.
[36] Y. Fan, J. Fang, X. Chang, M.-C. Tang, D. Barrit, Z. Xu, Z. Jiang, J. Wen, H. Zhao, T. Niu, D.-M. Smilgies, S. Jin, Z. Liu, E. Q. Li, A. Amassian, S. (F.) Liu, K. Zhao, *Joule* **2019**, *3*, 2485.
[37] Z. Zhang, R. Ji, M. Kroll, Y. J. Hofstetter, X. Jia, D. Becker-Koch, F. Paulus, M. Löffler, F. Nehm, K. Leo, Y. Vaynzof, *Adv. Energy Mater.* **2021**, *11*, 2100299.
[38] M. I. Pintor Monroy, I. Goldberg, K. Elkhouly, E. Georgitzikis, L. Clinckemalie, G. Croes, N. Annavarapu, W. Qiu, E. Debroye, Y. Kuang, M. B. J. Roeffaers, J. Hofkens, R. Gehlhaar, J. Genoe, *ACS Appl. Electron. Mater.* **2021**, *3*, 3023.
[39] G. Tong, T. Chen, H. Li, L. Qiu, Z. Liu, Y. Dang, W. Song, L. K. Ono, Y. Jiang, Y. Qi, *Nano Energy* **2019**, *65*, 104015.
[40] X. Chang, J. Fang, Y. Fan, T. Luo, H. Su, Y. Zhang, J. Lu, L. Tsetseris, T. D. Anthopoulos, S. (F.) Liu, K. Zhao, *Adv. Mater.* **2020**, *32*, 2001243.
[41] S. Y. Abate, Y. Qi, Q. Zhang, S. Jha, H. Zhang, G. Ma, X. Gu, K. Wang, D. Patton, Q. Dai, *Adv. Mater.* **2023**, *36*, 2310279.
[42] Z. Yang, W. Zhang, S. Wu, H. Zhu, Z. Liu, Z. Liu, Z. Jiang, R. Chen, J. Zhou, Q. Lu, Z. Xiao, L. Shi, H. Chen, L. K. Ono, S. Zhang, Y. Zhang, Y. Qi, L. Han, W. Chen, *Sci. Adv.* **2021**, *7*, eabg3749.
[43] Z. Liu, L. Qiu, E. J. Juarez-Perez, Z. Hawash, T. Kim, Y. Jiang, Z. Wu, S. R. Raga, L. K. Ono, S. Liu, Y. Qi, *Nat. Commun.* **2018**, *9*, 3880.
[44] J. Xi, C. Piao, J. Byeon, J. Yoon, Z. Wu, M. Choi, *Adv. Energy Mater.* **2019**, *9*, 1901787.
[45] J. Wang, S. Luo, Y. Lin, Y. Chen, Y. Deng, Z. Li, K. Meng, G. Chen, T. Huang, S. Xiao, H. Huang, C. Zhou, L. Ding, J. He, J. Huang, Y. Yuan, *Nat. Commun.* **2020**, *11*, 582.
[46] G. Uzurano, N. Kuwahara, T. Saito, A. Fujii, M. Ozaki, *ACS Mater. Lett.* **2022**, *4*, 378.
[47] X. Duan, X. Li, L. Tan, Z. Huang, J. Yang, G. Liu, Z. Lin, Y. Chen, *Adv. Mater.* **2020**, *32*, 2000617.
[48] B. Li, C. Zhang, D. Gao, X. Sun, S. Zhang, Z. Li, J. Gong, S. Li, Z. Zhu, *Adv. Mater.* **2023**, *36*, 2309768.
[49] Y. Qi, M. Almtiri, H. Giri, S. Jha, G. Ma, A. K. Shaik, Q. Zhang, N. Pradhan, X. Gu, N. I. Hammer, D. Patton, C. Scott, Q. Dai, *Adv. Energy Mater.* **2022**, *12*, 2202713.
[50] V. S. Katta, M. Waheed, J. H. Kim, *Sol. RRL* **2024**, *8*, 2300908.
[51] P. Makuła, M. Pacia, W. Macyk, *J. Phys. Chem. Lett.* **2018**, *9*, 6814.
[52] L. Yuan, S. Zou, K. Zhang, P. Huang, Y. Dong, J. Wang, K. Fan, M. Y. Lam, X. Wu, W. Cheng, R. Tang, W. Chen, W. Liu, K. S. Wong, K. Yan, *Adv. Mater.* **2024**, *36*, 2409261.
[53] Y. Lu, J. Hu, Y. Ge, B. Tian, Z. Zhang, M. Sui, *J. Mater. Chem. A* **2021**, *9*, 15059.
[54] K. Huang, Y. Peng, Y. Gao, J. Shi, H. Li, X. Mo, H. Huang, Y. Gao, L. Ding, J. Yang, *Adv. Energy Mater.* **2019**, *9*, 1901419.
[55] S. Park, D. W. Kim, S. Y. Park, *Adv. Funct. Mater.* **2022**, *32*, 2200437.
[56] S. Hu, K. Otsuka, R. Murdey, T. Nakamura, M. A. Truong, T. Yamada, T. Handa, K. Matsuda, K. Nakano, A. Sato, K. Marumoto, K. Tajima, Y. Kanemitsu, A. Wakamiya, *Energy Environ. Sci.* **2022**, *15*, 2096.
[57] M. Qin, K. Tse, T. Lau, Y. Li, C. Su, G. Yang, J. Chen, J. Zhu, U. Jeng, G. Li, H. Chen, X. Lu, *Adv. Mater.* **2019**, *31*, 1901284.
[58] P. Gratia, I. Zimmermann, P. Schouwink, J.-H. Yum, J.-N. Audinot, K. Sivula, T. Wirtz, M. K. Nazeeruddin, *ACS Energy Lett.* **2017**, *2*, 2686.
[59] D. P. McMeekin, P. Holzhey, S. O. Fürer, S. P. Harvey, L. T. Schelhas, J. M. Ball, S. Mahesh, S. Seo, N. Hawkins, J. Lu, M. B. Johnston, J. J. Berry, U. Bach, H. J. Snaith, *Nat. Mater.* **2022**, *22*, 73.
[60] H. X. Dang, K. Wang, M. Ghasemi, M.-C. Tang, M. De Bastiani, E. Aydin, E. Dauzon, D. Barrit, J. Peng, D.-M. Smilgies, S. De Wolf, A. Amassian, *Joule* **2019**, *3*, 1746.
[61] R. Roy, M. M. Byranvand, M. R. Zohdi, T. M. Friedlmeier, C. Das, W. Hempel, W. Zuo, M. Kedia, J. J. Rendon, S. Boehringer, *Energy Environ. Sci.* **2025**, *18*, 1920.

 © 2025 Wiley-VCH GmbH

16136829, 2025, 33, Downloaded from https://onlinelibrary.wiley.com/doi/10.1002/smll.202503825 by University Of Pennsylvania, Wiley Online Library on [06/10/2025]. See the Terms and Conditions (https://onlinelibrary.wiley.com/terms-and-conditions) on Wiley Online Library for rules of use; OA articles are governed by the applicable Creative Commons License

[62] X. Zheng, Y. Hou, C. Bao, J. Yin, F. Yuan, Z. Huang, K. Song, J. Liu, J. Troughton, N. Gasparini, C. Zhou, Y. Lin, D.-J. Xue, B. Chen, A. K. Johnston, N. Wei, M. N. Hedhili, M. Wei, A. Y. Alsalloum, P. Maity, B. Turedi, C. Yang, D. Baran, T. D. Anthopoulos, Y. Han, Z.-H. Lu, O. F. Mohammed, F. Gao, E. H. Sargent, O. M. Bakr, *Nat. Energy* **2020**, *5*, 131.

[63] T. Hellmann, C. Das, T. Abzieher, J. A. Schwenzer, M. Wussler, R. Dachauer, U. W. Paetzold, W. Jaegermann, T. Mayer, *Adv. Energy Mater.* **2020**, *10*, 2002129.

[64] J. P. Correa Baena, L. Steier, W. Tress, M. Saliba, S. Neutzner, T. Matsui, F. Giordano, T. J. Jacobsson, A. R. Srimath Kandada, S. M. Zakeeruddin, A. Petrozza, A. Abate, M. K. Nazeeruddin, M. Grätzel, A. Hagfeldt, *Energy Environ. Sci.* **2015**, *8*, 2928.

[65] M. A. Mahmud, T. Duong, Y. Yin, H. T. Pham, D. Walter, J. Peng, Y. Wu, L. Li, H. Shen, N. Wu, N. Mozaffari, G. Andersson, K. R. Catchpole, K. J. Weber, T. P. White, *Adv. Funct. Mater.* **2019**, *30*, 1907962.

[66] S. N. Habisreutinger, N. K. Noel, H. J. Snaith, R. J. Nicholas, *Adv. Energy Mater.* **2016**, *7*, 1601079.

[67] L. Hu, Q. Zhao, S. Huang, J. Zheng, X. Guan, R. Patterson, J. Kim, L. Shi, C.-H. Lin, Q. Lei, D. Chu, W. Tao, S. Cheong, R. D. Tilley, A. W. Y. Ho-Baillie, J. M. Luther, J. Yuan, T. Wu, *Nat. Commun.* **2021**, *12*, 466.

[68] W. Li, J. Liu, F.-Q. Bai, H.-X. Zhang, O. V. Prezhdo, *ACS Energy Lett.* **2017**, *2*, 1270.

[69] J. Xiong, P. N. Samanta, Y. Qi, T. Demeritte, K. Williams, J. Leszczynski, Q. Dai, *ACS Appl. Mater. Interfaces* **2022**, *14*, 5414.

[70] X. Sun, Z. Shao, Z. Li, D. Liu, C. Gao, C. Chen, B. Zhang, L. Hao, Q. Zhao, Y. Li, X. Wang, Y. Lu, X. Wang, G. Cui, S. Pang, *Joule* **2022**, *6*, 850.

[71] B. Li, Q. Zhang, S. Zhang, Z. Ahmad, T. Chidanguro, A. Hunter Davis, Y. C. Simon, X. Gu, W. Zheng, N. Pradhan, Q. Dai, *Chem. Eng. J.* **2021**, *405*, 126998.

[72] S. Y. Abate, Q. Zhang, Y. Qi, J. Nash, K. Gollinger, X. Zhu, F. Han, N. Pradhan, Q. Dai, *ACS Appl. Mater. Interfaces* **2022**, *14*, 28044.

[73] Y. Qi, K. A. Green, G. Ma, S. Jha, K. Gollinger, C. Wang, X. Gu, D. Patton, S. E. Morgan, Q. Dai, *Chem. Eng. J.* **2022**, *438*, 135647.

© 2025 Wiley-VCH GmbH

16136829, 2025, 33, Downloaded from https://onlinelibrary.wiley.com/doi/10.1002/smll.202503825 by University Of Pennsylvania, Wiley Online Library on [06/10/2025]. See the Terms and Conditions (https://onlinelibrary.wiley.com/terms-and-conditions) on Wiley Online Library for rules of use; OA articles are governed by the applicable Creative Commons License